SUPPORTING INFORMATION

SI MATERIALS AND METHODS

***Dictyostelium* constructs.** To obtain ForE-FL (aa 1-1,561) or ForEΔDAD (aa 1-1,511), genomic DNA of *Dictyostelium discoideum* AX2 WT cells was amplified by PCR and assembled in two steps in plasmid pJET1.2/blunt (ThermoFisher). After sequence verification (Dictybase accession number: DDB0231181), these vectors served as templates for all other ForE-derived plasmids. For expression of YFP-tagged ForE-FL or ForEΔDAD in *Dictyostelium*, corresponding fragments were amplified by PCR as BglII/SpeI fragments and inserted into the same sites of extrachromosomal expression plasmid pDM304-YFP (1). GFP-tagged ForAΔDAD (aa 1-1,138) was generated accordingly using pDGFP-MCS-Neo-ForAΔDAD (2) as template and inserted into pDM304-GFP (1). ForH-FL (aa 1-1,087) and ForHΔDAD (aa 1-1,053) were amplified from plasmid pDGFP-MCS-Neo-dDia2 (3) as a BamHI/SpeI fragment and inserted into the BglII/SpeI sites of plasmid pDM304-YFP (1). pDM304-GFP-Myo was generated by amplification of the sequence encoding myosin II heavy chain by PCR from plasmid pBIG-GFP-Myo (4), followed by insertion of obtained fragment into the BglII-SpeI sites of pDM304 (5). The F-actin probe LimEΔcoil-GFP for live cell imaging was generated accordingly using plasmid pDEXH-LimEΔcoil-GFP as template (6).

The *forE* targeting vector was constructed by amplification of a 0.5 kb 5′ PstI/BamHI fragment and a 0.5 kb 3′ SalI/HindIII fragment of the *forE* gene from genomic DNA following standard procedures. The fragments were successively inserted into the corresponding sites of pLPBLP (7). The *racA* and *racE* targeting vectors were constructed accordingly. The constructs for targeting the *forA* and *forH* genes were described previously (2, 3).

For expression of GST-tagged proteins in *E. coli*, *Dictyostelium* ForA-N (aa 139-548) was amplified from plasmid DNA and inserted into the BamHI/SalI sites of pGEX-6P-1 (GE Healthcare). ForA-C (aa 635-1218) was generated accordingly. The ForE-FH1FH2 domain (aa 1,042-1,511) was amplified from genomic DNA and inserted into the BamHI/SalI sites of pGEX-6P-1. RacA, RacE and mutant RacE-V20 were PCR-amplified from cDNA, plasmid or synthetic DNA and inserted into BamHI/SalI sites of pGEX-6P-1. All generated constructs were verified by sequencing.

Mammalian constructs. For generation of murine *Diaph1* (encoding mDia1) and *Diaph2* (encoding mDia3) targeting vectors, selected DNA target sequences (exon 3 in case of mDia1

and exon 1 in case of mDia3) were pasted into a CRISPR design tool (http://tools.genome-engineering.org). Predicted target sites with a high efficiency score were used for designing the sgRNA constructs (20 nucleotides). In case of mDia1, used target sequence was 5'-AGAAACTCCTCTGCATCGTA-3'. Genome editing of mDia3 was performed using guide #1: 5'-GAACCGGGCCGCCAACGAAG-3'. Respective sequences were ligated into expression plasmid pSpCas9(BB)-2A-Puro (PX459) V2.0 (Addgene plasmid ID: 62988) using BbsI (8). Plasmids pEGFP-C1-mDia1-FL (1-1,255) and pEGFP-C1-mDia1ΔDAD (1-1,179) were previously described (9). For generation of constitutively active, full length mDia1, a 430 bp fragment was removed at the 3' end after digestion with EcoRI and SalI and replaced by a synthetic fragment (BioCat) carrying the two amino substitutions M1182A and F1,195A shown to prevent tight interaction of the DAD with the GBD (10). EGFP-C1-mDia3 FL (1-1,102) was generated by amplification of the entire mouse cDNA as an XhoI-BamHI fragment and insertion of the fragment into the same sites of EGFP-C1. EGFP-C1-mDia3ΔDAD was made accordingly and encodes residues 1-1,052. For generation of constitutively active full length mDia3, a 1kp fragment at the 3' end was removed from EGFP-C1-mDia3 FL after digestion with AflII and BamHI and substituted with a synthetic fragment (BioCat) carrying the two amino substitutions M1057A and F1170A. For generation of recombinant mouse mDia1 antigen, pGEX-6P-1-mDia1N570 (1-570) was used (9). For expression of GST-tagged mouse mDia3 in *E. coli*, N-terminal sequences encoding the GBD-FH3 domain (104-485) were amplified from plasmid DNA and inserted into BamHI/SalI sites of pGEX-6P-1 (GE Healthcare). Validation of plasmids was confirmed by sequencing.

Cell Culture and Transfections. *D. discoideum* cells were grown in HL5-C medium including glucose (Formedium), either in shaken suspension at 150 rpm or on polystyrene petri dishes. The WT and mutant cells were transfected by electroporation using an Xcell gene pulser (Bio-Rad) using pre-set protocol 4-2-6 for *Dictyostelium*. The *forE*$^-$ cells were obtained by disruption of the *forE* gene in AX2 WT cells by homologous recombination using the pLPBLP-based targeting vector system (7) after digestion of the targeting vector with BamHI and SalI. The Blasticidin S resistance (Bsr) cassette in single formin-null cells was then removed by transient expression of Cre recombinase (7), and subsequently these strains were used to disrupt the remaining cortical formin genes to obtain *forA*$^-$/*forE*$^-$, *forA*$^-$/*forH*$^-$ and the *forE*$^-$/*forH*$^-$ double null mutants. Following the same strategy, the *forA*$^-$/*forE*$^-$/*forH*$^-$

triple mutant was generated. Stably transfected cells were selected with 10 µg·ml^{-1} Blasticidin S (Invivogen). Gene disruption was initially screened by PCR and finally confirmed by the absence of the respective formins in immunoblots. Cell lines expressing GFP- or YFP-tagged fusion proteins were obtained by transfecting the cells with the appropriate plasmids and selecting the transformants with 10 µg·ml^{-1} of geneticin (Sigma). Analysis of cytokinesis was performed with cells grown in shaken suspension at 150 rpm for 72 hours. For monitoring development, vegetative WT and mutant cells were harvested from growth medium, washed twice with 17 mM K/Na-phosphate buffer (PB), pH 6.0, and seeded with tooth picks on non-nutrient PB agar plates coated with a layer of *Klebsiella aerogenes*. After 96-120 h of incubation at 21 °C, the cells were imaged with a Nikon SMZ18 stereomicroscope equipped with a digital SLR DS-Ri2 camera and driven by NIS-Elements software.

Cell Culture, transfection and genome editing by CRISPR/Cas9 in B16-F1 mouse melanoma cells (ATCC CRL-6323) were performed essentially as described (11). Clonal cell lines devoid of mDia1, mDia3 and both mDia1/mDia3 were identified by immunoblotting using mDia1- and mDia3-specific sera, and confirmed to harbor accordingly disrupted genes by identification of frame shift mutations by sequencing after amplification of respective target sequences.

Protein Purification. Expression of GST-tagged fusion proteins was induced in *E. coli* strain Rossetta 2 (Novagen) with 1 mM isopropyl-ß-D-1-thiogalactoside (Roth) at 21 °C for 14 h. The proteins were subsequently purified from bacterial extracts by affinity chromatography using Protino glutathione-conjugated agarose 4B (Macherey-Nagel) followed by optional proteolytic cleavage with PreScission Protease (GE Healthcare), and a final polishing step by size-exclusion chromatography on an Äkta Purifier System using either HiLoad 26/600 Superdex 200 or HiLoad 26/600 Superdex 75 columns (GE Healthcare). The purified proteins were dialyzed against storage buffer (100 mM KCl, 2 mM dithiothreitol (DTT), 55% glycerol, and 20 mM Hepes, pH7.4) and stored at -20 °C for later use. The proteins used for immunization were dialyzed against immunization buffer (150 mM NaCl, 1 mM dithiothreitol (DTT), and 20 mM Tris/HCl pH7.4) and stored in aliquots at -20 °C. Actin was purified from acetone powder of rabbit skeletal muscle according to standard procedures (12), and labeled on Cys374 with N-(1-pyrenyl) maleimide (Invitrogen).

Pyrene and Pull-down Assays. Pyrene assays were performed as described previously (1). For GST binding assays, purified GST-RacE was bound to 250 µl of glutathione-conjugated agarose 4B beads in loading buffer (70 mM NaCl, 5 mM $MgCl_2$, 2 mM DTT, 2 mM benzamidine, 25 mM Tris/HCl, pH 7.5) and converted into the GDP- or GTP-bound forms by incubation of 400 µg of the protein for 30 min at 4°C with a 100-fold molar excess of either GDP or GMP-PNP (guanosine 5'-[β,γ-imido]triphosphate) in the presence of 5 mM EDTA. The reaction was stopped by the addition of $MgCl_2$ to a final concentration of 10 mM. For binding experiments, beads were washed once with loading buffer and incubated with 300 µg each of respective test proteins in 1 ml of loading buffer. After 1 hour of incubation at 4°C on a rotating wheel, beads were sedimented, washed five times with binding buffer, and bound proteins eluted with SDS sample buffer. Interactions were quantified by densitometry of Coomassie Blue stained gels after SDS-PAGE.

Antibodies Polyclonal antibodies against ForE (1,042-1,511), murine mDia1 (1-570) and mDia3 (104-485) were raised by immunizing a female New Zealand White rabbit with recombinant protein fragments devoid of the GST-tag following standard procedures. Immunoblotting was performed according to standard protocols using undiluted hybridoma supernatants of porin-specific mAb 70-100-1 (13), or polyclonal anti-ForA (2), ForH (3), ForE, mDia1 or mDia3 antibody sera (1:250 to 1:1,000 dilution). Anti-Glyceraldehyde-3-Phosphate Dehydrogenase (GAPDH) monoclonal antibody, clone 6C5 (1:1,000 dilution; no. MAB374) was from Merck Millipore. Primary antibodies in immunoblots were visualized with phosphatase-coupled anti-mouse (1:1,000, no. 115-055-62; Dianova) or anti-rabbit IgG (1:1,000; no. 111-055-046; Dianova). For immunofluorescence, anti-tubulin antibody YL1/2 (1:1,000, no ab6160; ThermoFisher) or undiluted hybridoma supernatants of CtxI-specific mAb 241-438-1 (14) and coronin-specific mAb 176-3-6 (15) were used. Primary antibodies in immunohistochemistry were visualized with Alexa Fluor 488-conjugated anti-mouse IgG (1:1,000 no A11029; Molecular Probes) or Alexa Fluor 546-conjugated anti-rat IgG (1:1,000 no A11081; Molecular Probes). The GFP signal was enhanced with Alexa488-conjugated nanobodies (1:200; no. gba488; Chromotek).

Fluorescence Microscopy and Imaging. For imaging of unconfined cells, cells were seeded onto 3-cm-diameter glass-bottom dishes (Ibidi) and allowed to adhere on the glass surface for 20 min. Cells were then washed four times with PB supplemented with 1% Trolox ((±)-6-hydroxy-2,5,7,8-tetramethylchromane-2-carboxylic acid, Sigma) and imaged using an Olympus IX81 microscope equipped with a 100x/1.3 UplanFl objective using GFP or YFP filter sets. For imaging in 2D-confinement, adherent cells were washed four times with PB supplemented with 1% Trolox, overlayed with a 0.17 µm thick slice of agar (1.5% in PB), and allowed to adapt to mechanical stress for 90-120 min prior to imaging. The topography of the ventral cell surface and cell-to-substratum contacts were imaged by RIC and DIC microscopy using the LSM 510 microscope and the 633-nm line of the He-Ne laser or by halogen lamp illumination, respectively. For immunofluorescence labeling, growth-phase cells were washed twice with PB and allowed to adhere on glass coverslips. Cells were fixed with picric acid/formaldehyde, permeabilized with 70% ethanol, and labeled for tubulin, Ctx I or coronin followed by Alexa Fluor 546-conjugated anti-rat IgG or Alexa Fluor 488-conjugated anti-mouse IgG. F-actin was visualized with Atto550-conjugated phalloidin (1:200; no AD550-81; ATTO-TEC). DNA was stained with TO-PRO3 (1:1,000; no T3605; Invitrogen). Cells were then imaged using an LSM510Meta confocal microscope (Zeiss) equipped with a 63x/1.3 Plan-Neofluar objective using the 488 nm, 543 nm and 633 nm laser lines. For the counting of nuclei, cells cultivated in shaken suspension for two days were fixed as described, and stained with 4',6-diamidino-2-phenylindole (DAPI). Specimens were analyzed using an Olympus IX81 microscope equipped with a 40x/0.75 UplanFl objective. Imaging of live or fixed B16-F1 and derived KO cell lines was performed as described (2, 11). Data were processed with Adobe PhotoShop, ImageJ and CorelDraw software.

Scanning Electron Microscopy. Cells were plated onto 13 mm diameter cleaned glass coverslips, pre-coated with Cell-Tak (Corning), and allowed to adhere for 3 hours. Cells were then washed in PB, before permeabilizing in cytoskeleton buffer (CB): 150 mM NaCl, 5 mM EGTA, 5mM $MgCl_2$, 5mM glucose, 10mM MES, pH 6.1 according to (16) containing 1% Triton X 100, 4% PEG (MW 35,000), and 2 µM phalloidin as described previously (17), for 3-5 mins. Cell permeabilization was monitored by imaging the cells using phase contrast microscopy. Cells were then washed with CB and stored in CB with 20 µM phalloidin before fixation with

2% glutaraldehyde in CB. Cells were postfixed with freshly prepared 0.1% tannic acid, followed by 0.2% uranyl acetate, and then critically point dried. Coverslips were mounted onto SEM stubs and coated with carbon to a thickness of < 10nm using the Quorum unit. Specimens were imaged using a Hitachi SUX230 high resolution FEG SEM and magnifications of 3-5K and 50K.

Micropipette Aspiration Assays. Micropipette aspiration was carried out as described (2). The set-up was described in detail previously (18). Briefly, a chamber with one open side was filled with 1 ml of PBS buffer and mounted on a stage of an inverted Axiovert 200 microscope (Carl Zeiss) equipped with a LD Achroplan 40x/0.6 objective (Carl Zeiss). A bovine serum albumin-coated glass micropipette with an inner diameter of 4.6 ± 1.3 µm was also filled with PBS buffer and positioned into the measurement chamber using a micromanipulator (Narishige). Aspiration pressure was applied with a height-adjustable water reservoir. The reference pressure (0 Pa) was calibrated by observing the motion of 2 µm polystyrene beads (Polysciences) in the pipette. After setting the pressure difference to 500 Pa, 50 µl of cell suspension was carefully injected into the chamber, and only non-adhering cells were aspirated. Aspiration was recorded using a sensicam qe CCD camera (PCO) with a frame rate of at least 2 Hz. Aspiration length (Lp) was determined using OpenBox (Informationssysteme Schilling) and Fiji software (19).

Myosin thickness and localization. GFP-myosin II intensity and localization in transfected WT and mutant cells in 2D-confinement under agar were analyzed by a custom-built macro for ImageJ software that allows to measure the intensity profiles along a rotating 1 pixel-wide line in 360°. The line was set to originate at the centroid and expands beyond the cell boundary. The collected data were further processed in Excel, to capture pixels with a higher intensity as compared to intracellular background fluorescence. The analysis was performed for twelve time points for each cell line. The obtained values for myosin II intensity were subsequently averaged and the mean myosin II band thickness for each angle was plotted in a polar plot in SigmaPlot (Systat).

Quantification of Actin Flow. WT and mutant cells expressing LimEΔcoil-GFP were imaged in 2D-confinement under agar with a Nikon Eclipse Ti-E inverted microscope equipped with a

TIRF Apo 100x/1.45 objective at 0.5 s intervals with exposure times of 40 ms using an Ixon3 897 EMCCD camera (Andor) for at least 10 min. Five consecutive frames from three different time-lapse movies per cell line were analyzed with PIVlab (20), a particle image velocimetry tool implemented in MatLab (MathWorks). The background was excluded from the analysis by the mask-tool in PIVlab and the received vector coordinates and u-v velocities were used to calculate magnitudes and draw vector fields on top of the cells. The velocity distribution histogram was generated with Excel (Microsoft) using a bin size of 4 $\mu m \cdot s^{-1}$ and plotted in SigmaPlot (Systat).

Analyses of Cell Migration. Quantitative analysis of *Dictyostelium* random cell motility and calculation of MSD was performed as described in detail previously (21). Random motility of B16-F1 cells and derived mDia knockout mutants was analyzed essentially as described (11).

Directional sensing assay. Directional sensing was assessed essentially as described (22). Briefly, WT cells expressing GFP- or YFP-tagged ForAΔDAD, ForEΔDAD and ForHΔDAD were harvested from axenic culture, seeded onto 3 cm-diameter glass-bottom dishes (Ibidi), and allowed to adhere on the glass surface for 30 min. Cells were then washed two times with PB supplemented with a bacterial suspension of *Klebsiella aerogenes* (OD_{600} 0.1) in PB containing 10 $\mu g\ ml^{-1}$ of G418 overnight to induce the chemotactic folate response system. Subsequently, cells were washed tree times with PB and exposed to 10 µM Latrunculin B (Enzo) for 10 min. A folate gradient was generated by a micropipette containing 10 µM folate. After establishment of the gradient, cells were examined by fluorescence microscopy using an Olympus IX81 microscope.

Y2H Assays. For protein-protein interaction studies, the MATCHMAKER GAL4 Two-Hybrid System 3 (Clontech Laboratories) was used. ForA-N (aa 139-548) was inserted into the pGADT7 prey vector to yield Gal4-activation domain-ForA-N. Likewise, ForE-N (aa 581-929) and ForH-N (aa 1-384) were inserted into pGADT7. All Rho family GTPases were inserted into the EcoRI and BamHI sites of the pGBKT7 bait vector, as described previously (1). The AH109 yeast strain was cotransfected with bait and prey vectors, and grown on synthetic double-dropout (DD) agar lacking leucine and tryptophan according to the manufacturer's

instructions. Several colonies were collected and grown in synthetic dropout liquid media overnight and then spotted onto dropout agar plates. Protein interactions were scored by growth of cells on agar plates for 4 d at 25 °C on triple-dropout (TD) or quadruple-dropout (QD) agar plates. TD plates lacked leucine, tryptophan, and histidine, and were supplemented with 3 mM 3-amino-1,2,4-triazole to suppress the leaky HIS3-reporter gene according to the manufacturer's instructions. QD plates lacked leucine, tryptophan, histidine, and adenine for screening at highest stringency.

Statistical Analyses. Statistical analyses were performed using SigmaPlot 11.2 software (Systat Software). Statistical significance of differences between non-normally distributed populations was determined by Mann-Whitney U test. When data fulfilled the criteria of normality (Shapiro–Wilk test) and equal variance (Levene's test), statistical differences were analyzed with a two-tailed, unpaired Student's t test. Statistical differences are reported as * $p<0.05$, ** $p<0.01$, ***$p < 0.001$ and n.s. as not significant.

Supplementary Figures:

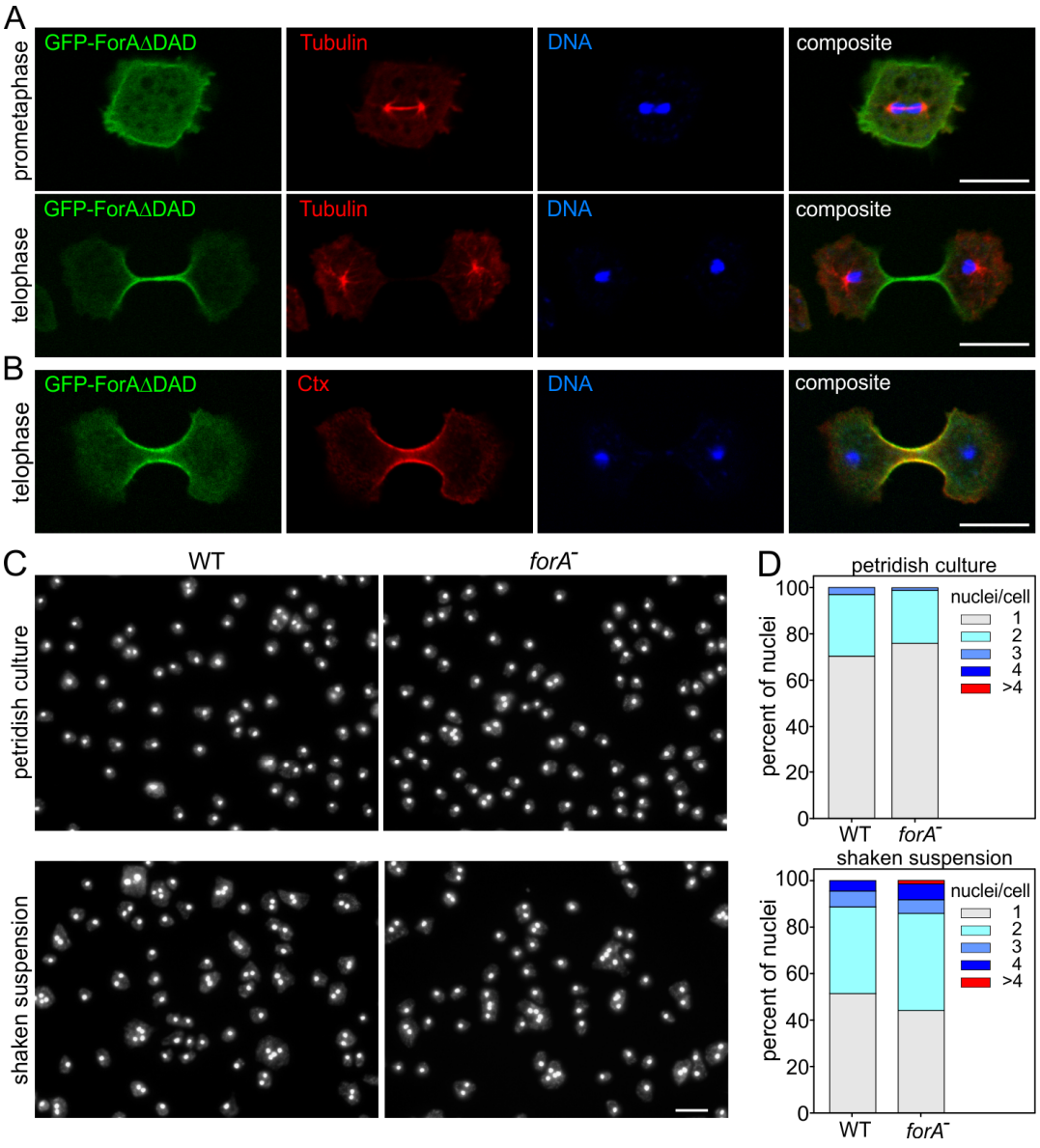

Fig. S1. Active ForA accumulates in the cleavage furrow of mitotic *Dictyostelium* cells, but *forA*⁻ cells exhibit no major defects in cytokinesis. (*A*) Cells expressing active, GFP-tagged ForA were fixed and stained with GFP-nanobodies to enhance the GFP signal. Tubulin was visualized with a monoclonal antibody, and DNA labelled with TO-PRO3. (*B*) The same cell line stained for GFP, Cortexillin (Ctx) and DNA to illustrate colocalization of ForA and Ctx in the cleavage furrow. Scale bars, 10 µm. (*C*) Elimination of ForA does not noticeably impair

cytokinesis of cells grown on petri dishes or cultivated in shaken suspension at 150 rpm for 48 h. Scale bar, 20 µm. (*D*) Quantification of nuclei per cell as shown in (C).

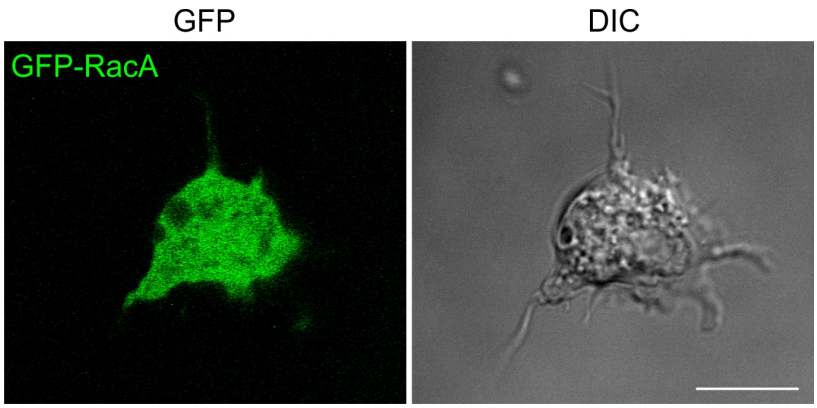

Fig. S2: GFP-tagged RacA is not targeted to the cell cortex and remains cytosolic. Epi-fluorescence and DIC images of a live *Dictyostelium* cell are shown. Scale bar, 10 µm.

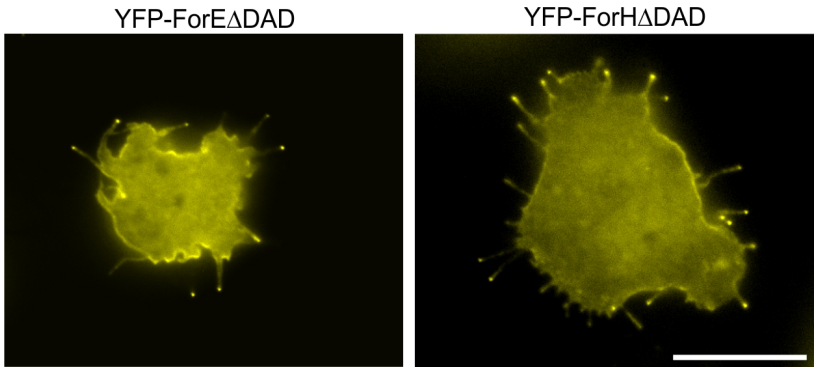

Fig. S3: Constitutively active ForE and ForH variants (ΔDAD) fused to YFP trigger the formation of numerous filopodia after expression in WT cells. Both formins accumulate at the cell cortex and the distal tips of filopodia. Epi-fluorescence images of live *Dictyostelium* cells are shown. Scale bar, 10 µm.

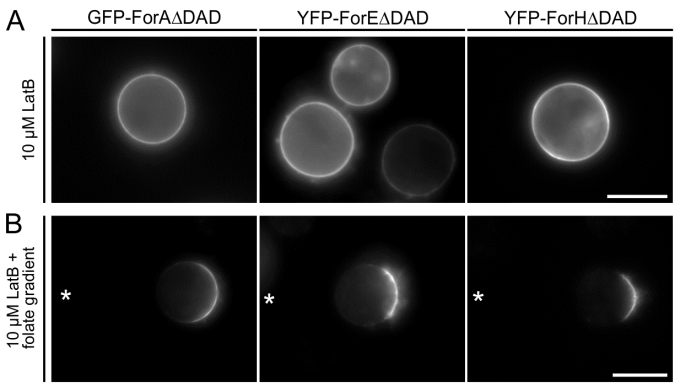

Fig. S4: Asymmetric localization of the cortical formins in an extracellular, chemical gradient. (*A*) WT *Dictyostelium* cells expressing indicated constructs were exposed to 10 µM Latrunculin B (LatB), and examined by fluorescence microscopy 10 min later. Note uniform cortical localization of constitutively active variants of ForA, ForE and ForH fused to GFP or YFP, as indicated, following depolymerization of the actin cytoskeleton by LatB. Virtually the same results were reported previously for RacE (23). (*B*) Gradient-sensing assay: WT *Dictyostelium* cells expressing indicated constructs were exposed to a folate gradient in the presence of 10 µM LatB. Images were taken after the folate gradient had formed. Asterisks indicate the position of micropipette tips releasing folate (10 µM). Constitutively active forms of ForA, ForE and ForH are located on the portion of the plasma membrane facing lower concentrations of chemoattractant, as demonstrated previously for active RacE (36). Scale bars, 10 µm.

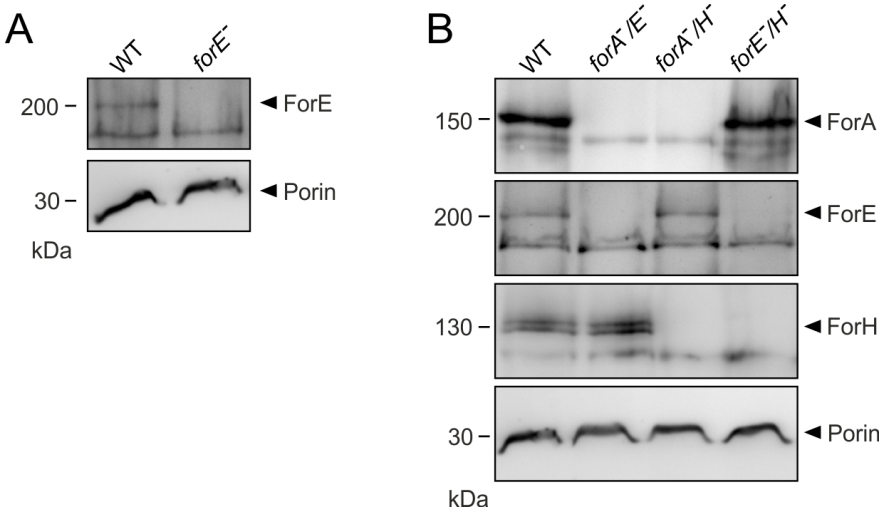

Fig. S5: Successful generation of the *forE*$^-$ single mutant (*A*) and of double mutants (*B*) lacking ForA, ForE or ForH in all possible combinations were confirmed to lack respective formins by SDS-PAGE and immunoblotting as indicated; Porin was used as loading control.

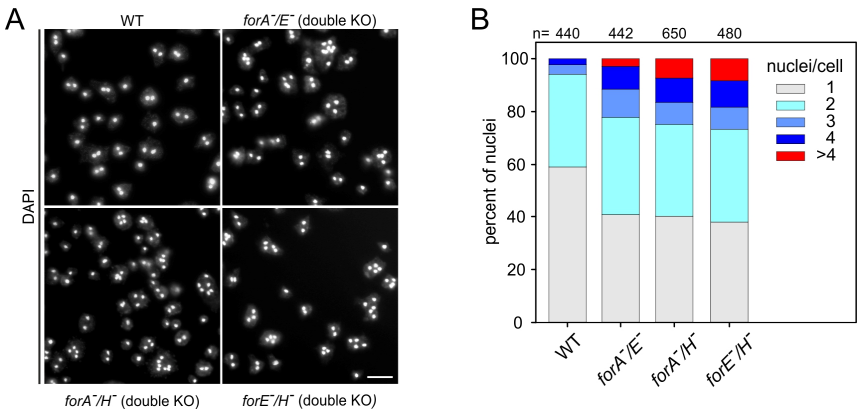

Fig. S6: *Dictyostelium* mutant cells devoid of two of the three cortical formins exhibited only moderate defects in cytokinesis. (*A*) WT and formin-double KO cells as indicated were grown for 48 h in shaken suspension at 150 rpm, followed by seeding on glass cover slips, fixation and staining with DAPI to visualize nuclei. Scale bar, 20 µm. (*B*) Quantification of nuclei of cells shown in (A); n, number of analyzed cells.

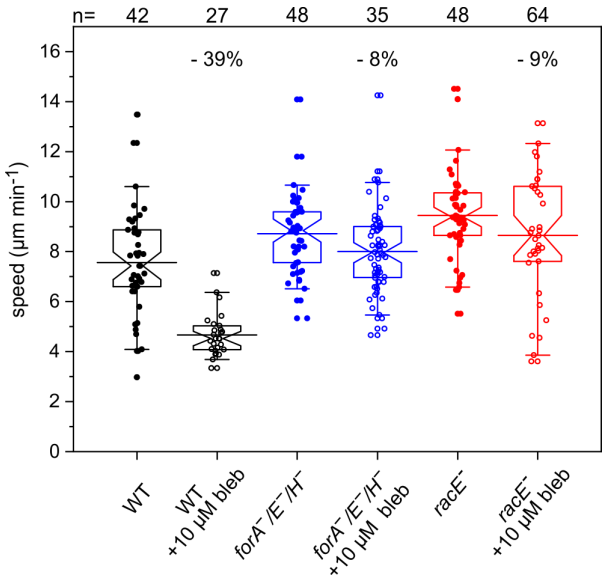

Fig. S7: Fast motility of unconfined *ForA⁻/E⁻/H⁻* and *racE⁻* mutant cells is not primarily driven by actomyosin contractility. Box plots summarizing migration speeds of freely migrating WT, *ForA⁻/E⁻/H⁻* and *racE⁻* cells in the absence or presence of 10 µM blebbistatin (bleb). While cell motility of WT cells was markedly reduced (by about 40%) upon blebbistatin addition, both mutants still migrated faster in the presence of the drug as compared to untreated control (WT). At least three movies each from three independent experiments were analyzed for all cell types; n, number of cells analyzed.

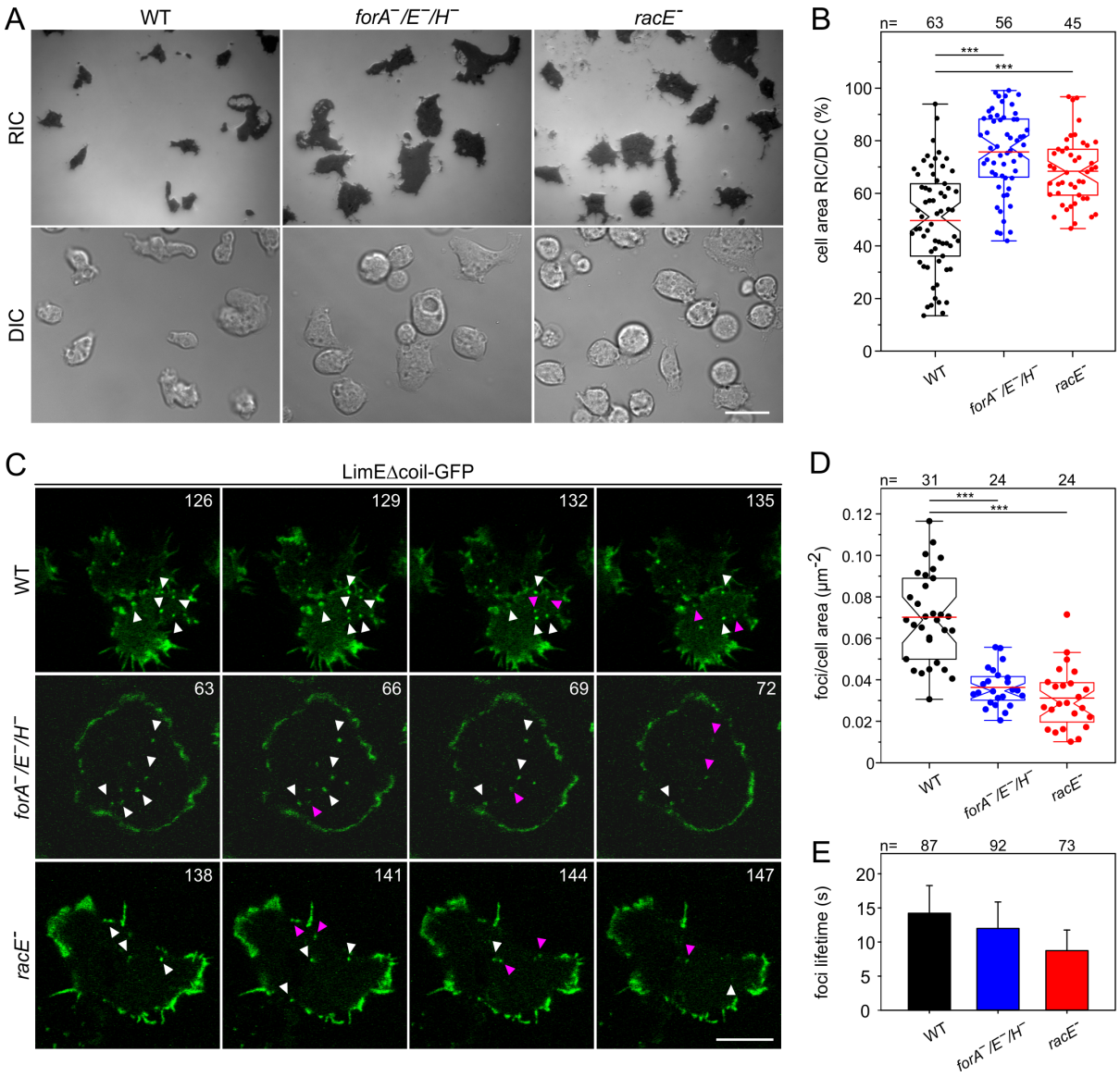

Fig. S8: Analyses of additional parameters potentially affecting *Dictyostelium* cell motility. (*A*) Micrographs of WT and mutant cells analyzed by differential interference contract (DIC) and reflection interference contrast (RIC) microscopy. Scale bar, 20 µm. (*B*) Box plots summarizing the substrate contact area of WT, *ForA⁻/E⁻/H⁻* and *racE⁻* cells. Representative stills from at least five independent experiments were analyzed for each cell type. n, number of cells analyzed. *** p<0.001 by Mann-Whitney rank sum test. Error bars, s.d.. (*C*) Confocal sections from time-lapse movies recorded close to the substratum of randomly migrating WT, *ForA⁻/E⁻/H⁻* and *racE⁻* cells expressing the actin probe LimEΔcoil-GFP. White arrow heads depict stable actin foci still present in the following frame, whereas magenta arrow heads point vanishing actin foci. Time is in s, scale bar, 10 µm. (*D*) Box plots displaying the number of foci per cell area of WT, *ForA⁻/E⁻/H⁻* and *racE⁻* cells. At least three movies each from three independent experiments were analyzed for all cell types. n, number of cells analyzed. *** p<0.001 by Mann-Whitney rank sum test. Error bars are s.d.. (*E*) Quantification of average lifetimes of actin foci in WT and mutant cells. Foci from at least

three movies each from three independent experiments were analyzed for all cell types. n, number of foci analyzed. Error bars show s.d..

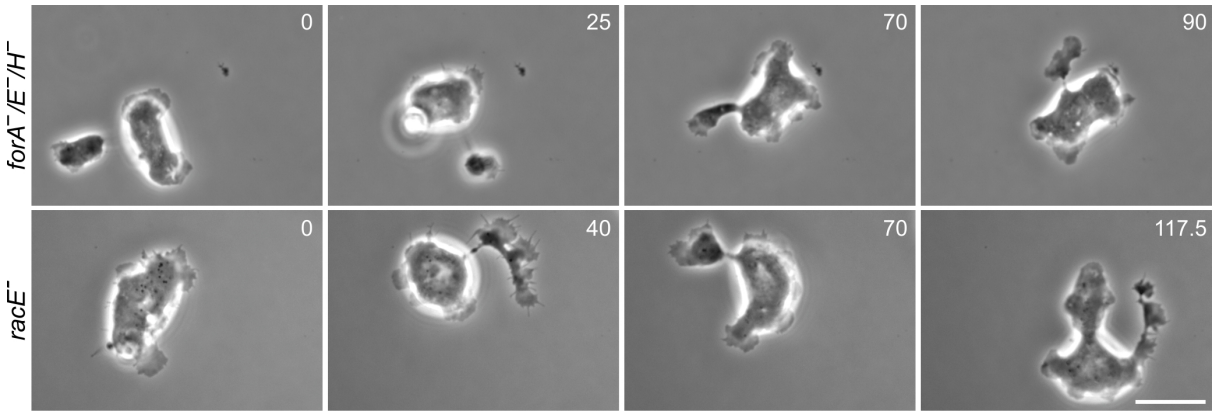

Fig. S9: Gallery with stills from phase-contrast time-lapse series of randomly migrating *Dictyostelium forA⁻/E⁻/H⁻* and *racE⁻* mutant cells in unconfined settings corresponding to Movie S8 shows repeated formation and absorption of small cell fragments derived from previous fronts and connected with the main cell body through thin, cytoplasmic threads. After losing contact with the substratum, these structures are rapidly retracted and internalized into the cell body. The process is likely caused by high load of the membrane due to the severely perturbed cortical cytoskeleton in the mutant cells. Time is in seconds; scale bar, 10 µm.

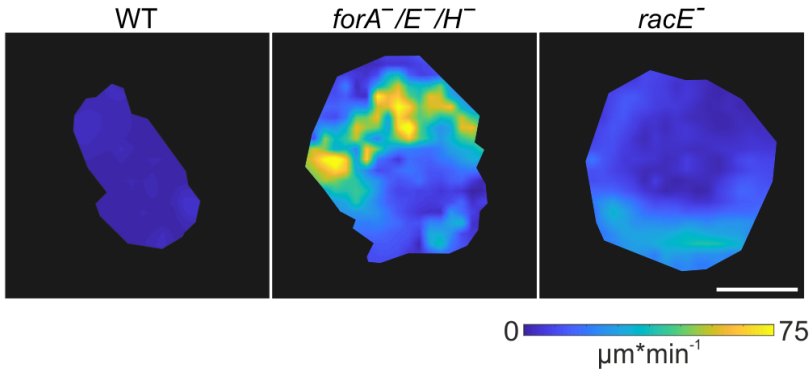

Fig. S10: Regions of fastest cortical actin flow in *Dictyostelium forA⁻/E⁻/H⁻* and *racE⁻* mutants, obtained by PIV analyses as shown in Fig. 7*D,* were detected in intracellular regions somewhat distant from the cell periphery. These data suggest these regions to represent the ectoplasm-endoplasm boundary, which is strongly enriched for myosin II (shown in Fig. 7*A*). By contrast, WT cells exhibited an only slightly enhanced actin flow at protruding fronts. Velocities of cortical flows are color-coded, as indicated at the bottom right. Scale bar, 10 µm.

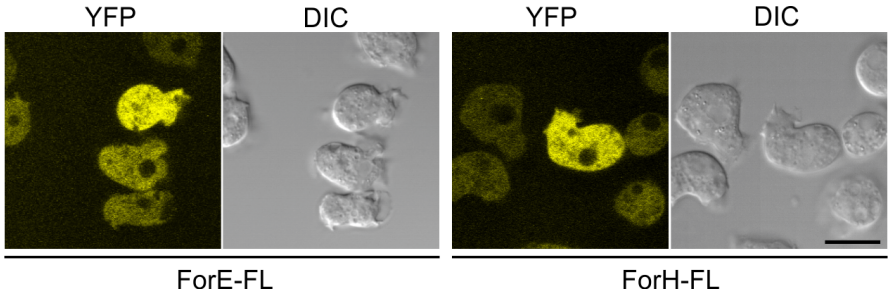

Fig. S11. YFP-tagged full-length (FL) ForE and ForH are entirely cytoplasmic and thus autoinhibited. Transfected *Dictyostelium* WT cells expressing indicated constructs were imaged on 3 cm glass-bottom dishes in PB buffer by confocal microscopy using 488 nm laser excitation and DIC imaging. Scale bar, 10 µm. Virtually identical results were obtained previously for cells expressing GFP-tagged full-length ForA (2).

Supplemental Movie Legends:

Movie Legends

Movie S1. Constitutively active RacE-V20 fused to YFP accumulates in the trailing cortex of *Dictyostelium* cells migrating in 2D-confinement under agar. WT cells expressing YFP-RacE-V20 were imaged on 3 cm glass-bottom dishes in PB buffer by fluorescence microscopy at 40x magnification. Time is in min:s; scale bar, 10 µm.

Movie S2. Aspiration of *Dictyostelium* WT and mutant cells at 500 Pa in PB buffer. At a stable suction pressure of 500 Pa, the initial dilation length of *forA⁻/E⁻/H⁻* and *racE⁻* cells is considerably larger than that observed for WT control. However, similar to WT, *racE⁻* cells were able to withstand the suction pressure, while the majority of *forA⁻/E⁻/H⁻* cells (98%) were completely sucked in. Time is in min:s; Scale bar, 10 µm.

Movie S3. Cortical defects in *Dictyostelium forA⁻/E⁻/H⁻* and *racE⁻* mutant cells. WT and mutant cells expressing the F-actin sensor LimEΔcoil-GFP were imaged on 3 cm glass-bottom dishes in PB buffer at 4.5 seconds intervals by confocal microscopy using a 488 nm laser line and 63x objective. Note the homogenous rim of cortical actin in protrusion-free areas in WT cells, which is contrasted by prominent regions devoid of cortical F-actin in the mutants. Time is in min:s; scale bar, 10 µm.

Movie S4. Highly directional movement of fan-shaped *Dictyostelium forA⁻/E⁻/H⁻* and *racE⁻* cells. WT and respective mutant cells were recorded by phase-contrast imaging in PB using 10x objective, and tracked as indicated. Time is in min:s; scale bar, 50 µm.

Movie S5. Freely migrating *Dictyostelium ForA⁻/E⁻/H⁻* and *racE⁻* cells display pronounced formation of multiple fronts as compared to WT cells. Cells were recorded by phase-contrast imaging in HL5C medium using a 100x objective. Time is in min:s; scale bar, 10 µm.

Movie S6. Dynamic behavior of *ForA⁻/E⁻/H⁻* and *racE⁻ Dictyostelium* cells displaying multiple fronts. Cells were imaged on 3 cm glass-bottom dishes in PB buffer at 3.5 second intervals by RIC imaging using a 633 nm laser line and 63x objective. Note vanishing cell adhesion prior to retraction of previously formed fronts. Time is in min:s; scale bar, 10 µm.

Movie S7. Substrate adhesion is reduced in *Dictyostelium racE⁻* mutant cells utilizing the fish keratocyte-like motility mode. Representative cell imaged on 3 cm glass-bottom dish in PB buffer at 3.5 second intervals by RIC and DIC microscopy using a 63x objective as well as a 633 nm laser line and halogen lamp illumination, respectively. Note that white spotty regions correspond to prominent gaps in contact area. Time is in min:s, scale bar, 10 µm.

Movie S8. Highly dynamic behavior of freely migrating *Dictyostelium ForA⁻/E⁻/H⁻* and *racE⁻* cells. Note that protrusion of initially formed fronts in the mutants typically ceased when multiple, competing fronts were formed on the opposite side of the cell. In these cases, initially formed fronts subsequently lost adhesion to the underlying substratum and were effectively retracted into the cell body, likely due to limited membrane surface in the absence of an intact viscoelastic cell cortex. Cells were imaged by phase contrast, time-lapse microscopy in HL5C medium using a 100x objective. Time is in min:s; scale bar, 10 µm.

Movie S9. ForA/E/H- and RacE-deficient *Dictyostelium* cells cannot polarize effectively. WT, *ForA⁻/E⁻/H⁻* and *racE⁻* cells expressing the heavy chain of myosin II fused to GFP were imaged on 3 cm glass-bottom dishes in PB buffer by widefield fluorescence microscopy using a 100x objective. Time is in min:s; scale bar, 10 µm.

Movie S10. Cortical actin flow is drastically increased in *forA⁻/E⁻/H⁻* and *racE⁻* mutants as compared to WT *Dictyostelium* cells in the 2D-confined setting. Cells expressing the F-actin probe LimEΔcoil-GFP were imaged on 3 cm glass-bottom dishes in PB buffer at 2 Hz intervals using TIRF-microscopy with a 488 nm laser line and 100x objective. Time is in seconds; scale bar, 10 μm.

References

1. Junemann A, et al. (2016) A *Diaphanous* -related formin links Ras signaling directly to actin assembly in macropinocytosis and phagocytosis. *Proc Natl Acad Sci* 113(47):E7464–E7473.

2. Ramalingam N, et al. (2015) A resilient formin-derived cortical actin meshwork in the rear drives actomyosin-based motility in 2D confinement. *Nat Commun* 6. doi:10.1038/ncomms9496.

3. Schirenbeck A, Bretschneider T, Arasada R, Schleicher M, Faix J (2005) The Diaphanous-related formin dDia2 is required for the formation and maintenance of filopodia. *Nat Cell Biol* 7(6). doi:10.1038/ncb1266.

4. Levi S, Polyakov M V, Egelhoff TT (2002) Myosin II dynamics in Dictyostelium: determinants for filament assembly and translocation to the cell cortex during chemoattractant responses. *Cell Motil Cytoskeleton* 53(3):177–88.

5. Veltman DM, Keizer-Gunnink I, Haastert PJM Van (2009) An extrachromosomal, inducible expression system for Dictyostelium discoideum. *Plasmid* 61(2):119–125.

6. Schneider N, et al. (2003) A Lim protein involved in the progression of cytokinesis and regulation of the mitotic spindle. *Cell Motil Cytoskeleton* 56(2). doi:10.1002/cm.10139.

7. Linkner J, Nordholz B, Junemann A, Winterhoff M, Faix J (2012) Highly effective removal of floxed Blasticidin S resistance cassettes from Dictyostelium discoideum mutants by extrachromosomal expression of Cre. *Eur J Cell Biol* 91(2):156–60.

8. Ran FA, et al. (2013) Genome engineering using the CRISPR-Cas9 system. *Nat Protoc* 8(11):2281–2308.

9. Ramalingam N, et al. (2010) Phospholipids regulate localization and activity of mDia1 formin. *Eur J Cell Biol* 89(10):723–732.

10. Lammers M, Rose R, Scrima A, Wittinghofer A (2005) The regulation of mDia1 by autoinhibition and its release by Rho*GTP. *EMBO J* 24(23):4176–87.

11. Kage F, et al. (2017) FMNL formins boost lamellipodial force generation. *Nat Commun* 8. doi:10.1038/ncomms14832.

12. Spudich JA, Watt S (1971) The regulation of rabbit skeletal muscle contraction. I. Biochemical studies of the interaction of the tropomyosin-troponin complex with actin and the proteolytic fragments of myosin. *J Biol Chem* 246(15):4866–71.

13. Troll H, et al. (1992) Purification, functional characterization, and cDNA sequencing of mitochondrial porin from Dictyostelium discoideum. *J Biol Chem* 267(29):21072–9.

14. Faix J, et al. (1996) Cortexillins, major determinants of cell shape and size, are actin-bundling proteins with a parallel coiled-coil tail. *Cell* 86(4). doi:10.1016/S0092-8674(00)80136-1.

15. de Hostos EL, Bradtke B, Lottspeich F, Guggenheim R, Gerisch G (1991) Coronin, an actin binding protein of Dictyostelium discoideum localized to cell surface projections, has sequence similarities to G protein beta subunits. *EMBO J* 10(13):4097–104.

16. Small JV, Rottner K, Hahne P, Anderson KI (1999) Visualising the actin cytoskeleton. *Microsc Res Tech* 47(1):3–17.

17. Svitkina TM (2009) Imaging Cytoskeleton Components by Electron Microscopy. *Methods in Molecular Biology (Clifton, N.J.)*, pp 187–206.

18. Dieluweit S, et al. (2010) Mechanical Properties of Bare and Protein-Coated Giant Unilamellar Phospholipid Vesicles. A Comparative Study of Micropipet Aspiration and Atomic Force Microscopy. *Langmuir* 26(13):11041–11049.

19. Schindelin J, et al. (2012) Fiji: an open-source platform for biological-image analysis.

Nat Methods 9(7):676–682.

20. Thielicke W, Stamhuis EJ (2014) PIVlab – Towards User-friendly, Affordable and Accurate Digital Particle Image Velocimetry in MATLAB. *J Open Res Softw* 2:e30.

21. Litschko C, et al. (2017) Differential functions of WAVE regulatory complex subunits in the regulation of actin-driven processes. *Eur J Cell Biol*. doi:10.1016/j.ejcb.2017.08.003.

22. Aufderheide KJ, Janetopoulos C (2016) Migration of Dictyostelium discoideum to the Chemoattractant Folic Acid. *Methods in Molecular Biology (Clifton, N.J.)*, pp 25–39.

23. Wang Y, Senoo H, Sesaki H, Iijima M (2013) Rho GTPases orient directional sensing in chemotaxis. *Proc Natl Acad Sci* 110(49):E4723–E4732.